nature communications

Article

https://doi.org/10.1038/s41467-025-63580-2

Magnetic imaging under high pressure with a spin-based quantum sensor integrated in a van der Waals heterostructure

Received: 26 January 2025

Accepted: 20 August 2025

Published online: 29 September 2025

Check for updates

Z. Mu[1], J. Fraunié[2], A. Durand[1], S. Clément[1], A. Finco[1], J. Rouquette[3], A. Hadj-Azzem[4], N. Rougemaille[4], J. Coraux[4], J. Li[5], T. Poirier[5], J. H. Edgar[5], I. C. Gerber[2], X. Marie[2,6], B. Gil[1], G. Cassabois[1,6], C. Robert[2] & V. Jacques[1]

Pressure is a powerful tool for tuning the magnetic properties of van der Waals magnets owing to their weak interlayer bonding. However, local magnetometry measurements under high pressure still remain elusive for this important class of emerging materials. Here we demonstrate magnetic imaging of a van der Waals magnet under high pressure with sub-micron spatial resolution, using a two-dimensional (2D) quantum sensing platform based on boron-vacancy (V_B^-) centers in hexagonal boron nitride (hBN). We first analyze the performances of V_B^- centers in hBN for magnetic imaging under pressures up to few GPa, and we then use this 2D sensing platform to investigate the pressure-dependent magnetization in micrometer-sized flakes of 1*T*-$CrTe_2$. Besides providing a new path for studying pressure-induced phase transitions in van der Waals magnets, this work also opens up interesting perspectives for exploring the physics of 2D superconductors under pressure via local measurements of the Meissner effect.

Magnetic van der Waals materials and their associated heterostructures are currently attracting considerable interest, both for the study of magnetic order in two-dimensional (2D) systems and for the design of atomically-thin spintronic devices[1–3]. Due to their lamellar structure with weak interlayer bonding, the properties of van der Waals magnets are very sensitive to pressure. For example, a transition from antiferromagnetic to ferromagnetic interlayer coupling is achieved for thin exfoliated flakes of CrI_3 at a pressure of few GPa, owing to a structural transition from monoclinic to rhombohedral layer stacking[4,5]. Pressure can also be used to tune the Curie temperature as well as the balance between exchange interactions and magneto-crystalline anisotropies in a broad variety of van der Waals magnets[6–10]. Such an efficient control of magnetic interactions with pressure opens up interesting prospects for the design of exotic magnetic phases in van der Waals heterostructures. However, these studies are hampered by a lack of experimental methods providing in situ magnetic imaging of micrometer-sized samples under pressure, a notoriously difficult task in high pressure science and technology.

A powerful approach to magnetic imaging under pressure with high sensitivity and sub-micron spatial resolution relies on the integration of a spin-based quantum sensor into a diamond anvil cell (DAC), which is the most widely used device to generate high hydrostatic pressure environments [Fig. 1a]. A prominent example is the use of nitrogen-vacancy (NV) centers implanted near the surface of a diamond anvil to probe magnetic signals generated inside the high-pressure chamber of a DAC via optically detected magnetic resonance (ODMR) methods[11–17]. Here we explore an alternative solution based on boron-vacancy (V_B^-) centers in hexagonal boron nitride (hBN), which is

[1]Laboratoire Charles Coulomb, Université de Montpellier and CNRS, Montpellier, France. [2]Université de Toulouse, INSA-CNRS-UPS, LPCNO, 135 Avenue Rangueil, Toulouse, France. [3]Institut Charles Gerhardt, Université de Montpellier and CNRS, Montpellier Cedex, France. [4]Université Grenoble Alpes, CNRS, Grenoble INP, Institut NEEL, Grenoble, France. [5]Tim Taylor Department of Chemical Engineering, Kansas State University, Kansas, USA. [6]Institut Universitaire de France, Paris, France. e-mail: vincent.jacques@umontpellier.fr

https://doi.org/10.1038/s41467-025-63580-2

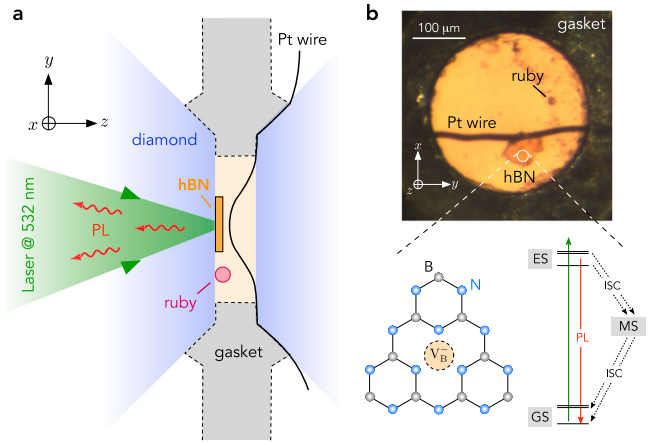

Fig. 1 | Principle of the experiment. a Sketch of the experimental arrangement combining a membrane-driven DAC with a scanning confocal microscope. **b** Optical image of the sample chamber of the DAC showing a micrometer-thick neutron-irradiated hBN crystal, a platinum (Pt) wire used for microwave excitation and a ruby crystal for local pressure measurements. Bottom panels: Atomic structure and simplified energy level diagram of the V_B^- center in hBN, showing the optical transition between the spin triplet ground (GS) and excited (ES) states driven by a green laser excitation, and non-radiative intersystem-crossing (ISC) transitions to a metastable (MS) singlet state.

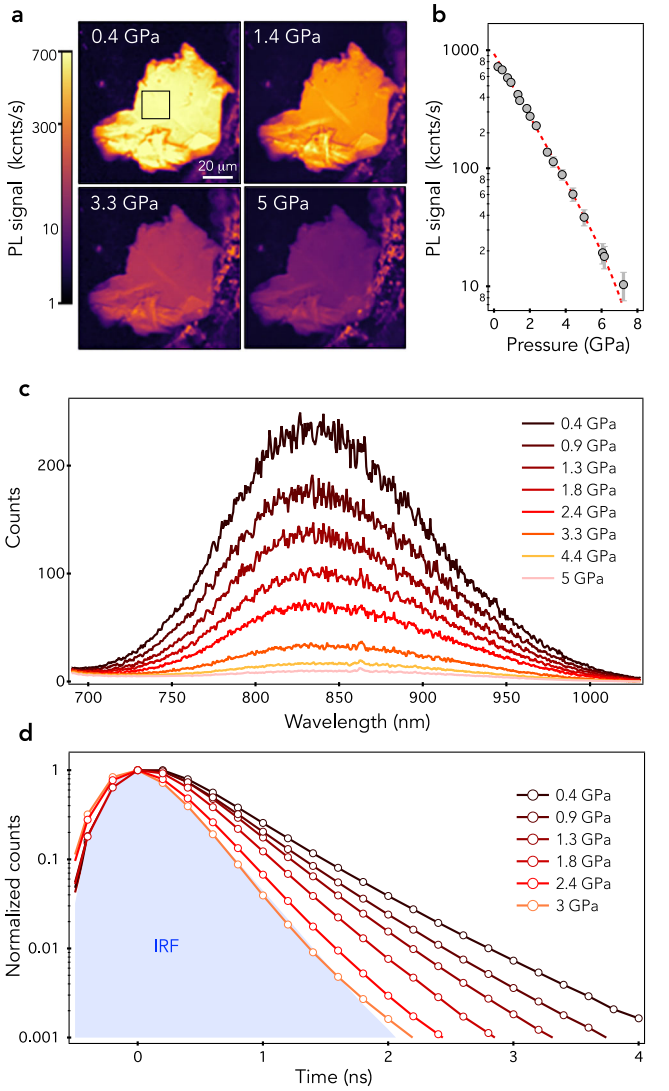

Fig. 2 | Optical properties of V_B^- centers in hBN under hydrostatic pressure. a PL raster scans of the hBN crystal recorded at different pressures using a green laser power of 1 mW. **b** PL signal averaged within the black square shown in (**a**) as a function of pressure. The error bars correspond to one standard deviation uncertainty. **c** Series of PL spectra and (**d**) time-resolved PL decays of V_B^- centers recorded at different pressures. The shaded area in (**d**) corresponds to the instrument response function (IRF) of the photon counting system measured with 60-ps laser pulses.

a promising platform for magnetic imaging in van der Waals heterostructures[18–21]. Similar to the NV defect in diamond, the V_B^- center in hBN features a spin triplet ground state whose electron spin resonance frequencies can be interrogated by ODMR spectroscopy[18], a key resource for quantum sensing and imaging technologies. Importantly, V_B^- centers hosted in thin hBN layers can be easily integrated into van der Waals heterostructures, providing atomic-scale proximity between the spin-based quantum sensor and any type of 2D material.

In this work, we demonstrate that V_B^- centers in hBN can be used for magnetic imaging in van der Waals heterostructures under high pressure with sub-micron spatial resolution. The novelty of our results is twofold. First, we analyze the impact of hydrostatic pressure on the magneto-optical properties of V_B^- centers hosted in a bulk hBN crystal. We show that the ODMR response of the V_B^- center is preserved up to pressures of a few GPa despite a strong pressure-induced enhancement of non-radiative decay rates in optical cycles. We infer a global hydrostatic shift of the V_B^- center's electron spin resonance frequencies of ~48 MHz/GPa, a value in very good agreement with recent first-principles calculations[22]. Second, we integrate V_B^- centers into a van der Waals heterostructure involving a 2D magnet and we demonstrate in situ magnetic imaging under pressure. As a proof of concept, we study the pressure-dependent magnetization in micrometer-sized flakes of 1*T*-$CrTe_2$, a van der Waals ferromagnet with in-plane magnetic anisotropy and a Curie temperature T_c ~320 K at ambient pressure[23–26].

Results and discussion

Principle of the experiment

We start by studying how the optical and spin properties of V_B^- centers in hBN evolve with pressure. To this end, we rely on a monoisotopic $h^{10}BN$ crystal in which V_B^- centers are created through neutron irradiation[27–29] (Methods). As sketched in Fig. 1(a), a piece of this bulk hBN crystal is loaded into the sample chamber of a membrane-driven DAC, which is defined by a hole drilled in a rhenium gasket that is compressed by two opposing diamond anvils. The sample chamber is filled with a pressure-transmitting medium, consisting of NaCl or Daphne oil[30], to provide a quasi-hydrostatic pressure environment and a ruby crystal is used as a local pressure gauge[31] (see Supplementary Fig. 1). The optical response of V_B^- centers under pressure is studied at room temperature with a scanning confocal microscope employing a green laser excitation, a long-working distance objective with a numerical aperture NA = 0.42 and a photon counting module (Methods). To perform ODMR spectroscopy, a microwave excitation is applied through a platinum wire crossing the DAC chamber [Fig. 1(b)].

Optical properties of V_B^- centers in hBN under pressure

Photoluminescence (PL) raster scans of the neutron-irradiated hBN crystal recorded at different pressures are shown in Fig. 2a. The PL signal of V_B^- centers is drastically reduced with increasing pressure and becomes almost undetectable above 7 GPa [Fig. 2b]. This behavior is confirmed by measurements of PL spectra, which feature the characteristic broadband emission of V_B^- centers in the near infrared with an intensity decreasing with pressure [Fig. 2c]. The process is reversible, the PL signal being recovered when pressure is released. To gain insight into the mechanism underlying this pressure-induced PL

https://doi.org/10.1038/s41467-025-63580-2

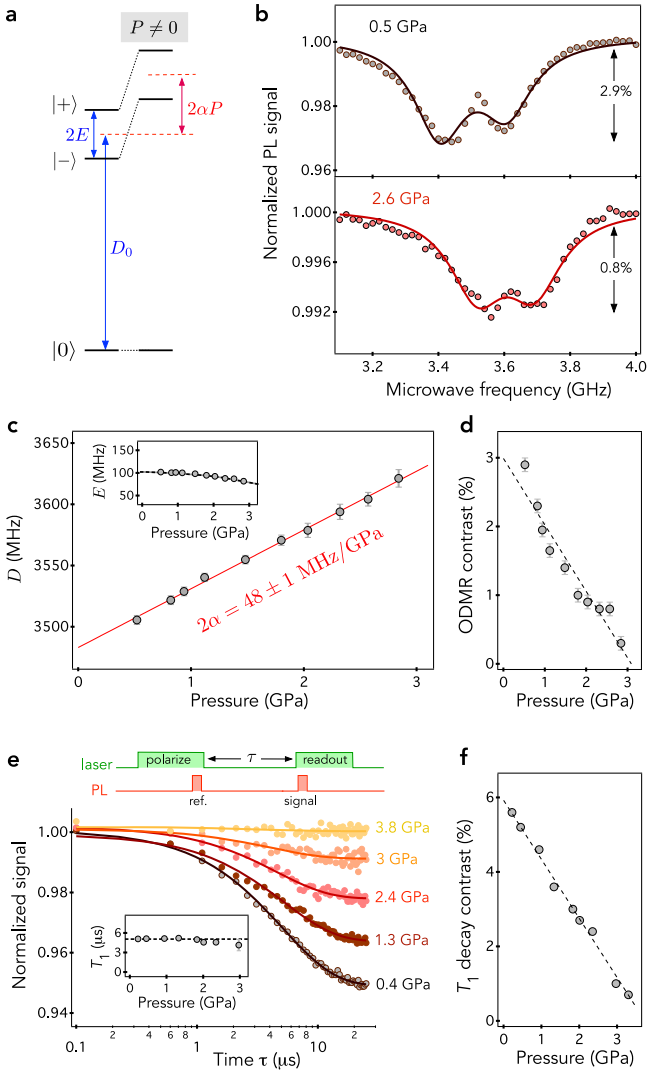

Fig. 3 | Spin properties under hydrostatic pressure. a Energy level structure of the spin triplet ground state illustrating the impact of hydrostatic pressure P. All notations are defined in the main text. **b** ODMR spectra recorded at 0.5 GPa (top) and 2.6 GPa (bottom). The solid lines are data fitting with Lorentzian functions from which the parameter D and E are extracted. **c** Zero-field splitting parameter D as a function of P. The solid line is a fit with a linear function yielding $2\alpha = 48 \pm 1$ MHz/GPa. Inset: Evolution of the E-splitting parameter with P. The dashed line is a guide for the eye. **d** ODMR contrast as a function of P. The error bars in (**d**) and (**e**) correspond to one standard error in the fitting of ODMR spectra with Lorentzian functions. **e** Optically-detected spin relaxation curves recorded at different pressures using the experimental pulse sequence shown on top. The solid lines are data fitting with an exponential decay (see "Methods"). Inset: Evolution of the spin relaxation time T_1 with P. **f** Contrast of the spin relaxation decay as a function of P. All experiments are performed at the same laser excitation power of 1 mW.

quenching, the lifetime of the V_B^- center's excited state was measured using a pulsed laser source. After optical excitation, the relaxation of V_B^- centers is dominated by non-radiative decay channels involving intersystem crossing (ISC) to a metastable state [Fig. 1b]. These processes lead to an excited-state lifetime on the order of ~1 ns under ambient conditions, the precise value of which depends on the density of V_B^- centers, the quality of the hBN crystal and the method used to create V_B^- centers[32–35]. In our neutron-irradiated hBN crystal, the excited-state lifetime is around 0.6 ns under ambient conditions. Time-resolved PL decays recorded at different pressures indicate that the excited-state lifetime is significantly reduced with increasing pressure [Fig. 1d]. A quantitative analysis of this effect can hardly be performed since the PL decay of V_B^- centers cannot be distinguished from the instrument response function (IRF) of our photon counting module (~300 ps) for pressure above 2 GPa. However, these measurements clearly indicate that pressure-induced PL quenching is linked to an enhancement of non-radiative decay rates in the optical cycles of V_B^- centers.

Electron spin properties of V_B^- centers in hBN under pressure

We then investigate the impact of hydrostatic pressure on the spin triplet ground state (S = 1) of the V_B^- center, whose Hamiltonian is expressed in frequency units as

$$\hat{\mathcal{H}} = D_0 \hat{S}_z^2 + E(\hat{S}_x^2 - \hat{S}_y^2) + \hat{\mathcal{H}}_s \,, \tag{1}$$

where $\{\hat{S}_x, \hat{S}_y, \hat{S}_z\}$ are the dimensionless electron spin operators. The first term describes the spin-spin interaction that leads to an axial zero-field splitting D_0 ~3.47 GHz at ambient pressure between the $|m_s = 0\rangle$ and $|m_s = \pm 1\rangle$ spin sublevels[18], where m_s denotes the electron spin projection along the c axis (z) of the hBN crystal. The second term results from the coupling of the V_B^- center with a local electric field produced by surrounding charges[22,36,37]. As sketched in Fig. 3a, this interaction mixes the $|m_s = \pm 1\rangle$ spin sublevels, leading to new eigenstates $|\pm\rangle$ separated by an orthorhombic splitting $2E$, whose amplitude is linked to the volumic density of charges in the hBN crystal that increases with the density of V_B^- centers[22,36]. Finally, the third term $\hat{\mathcal{H}}_s$ describes the spin-stress coupling. Considering a hydrostatic pressure environment, the stress tensor is diagonal with identical principal components $\sigma_{xx} = \sigma_{yy} = \sigma_{zz} = P$, where P is the applied pressure. The electron spin density of the V_B^- center is mainly localized in the (x, y) plane[38,39]. Since the stress component σ_{zz} has a small impact on the in-plane hBN structure, its coupling to the V_B^- center can be safely neglected. In this framework, the Hamiltonian term describing the effect of hydrostatic pressure can be simply written as[22]

$$\hat{\mathcal{H}}_s = \alpha(\sigma_{xx} + \sigma_{yy})\hat{S}_z^2 = 2\alpha P \hat{S}_z^2 \,, \tag{2}$$

where α denotes the stress coupling coefficient. Hydrostatic pressure thus leads to a global shift of the $|\pm\rangle$ spin sublevels, resulting in an increase of the zero-field splitting parameter $D = D_0 + 2\alpha P$ [Fig. 3a].

Typical ODMR spectra recorded at two different pressures are shown in Fig. 3b. We detect the characteristic magnetic resonances of the V_B^- spin triplet ground state with frequencies given by $\nu_\pm = D \pm E$, which are shifted to higher frequency upon increasing pressure. The variation of the zero-field splitting parameter D with pressure is plotted in Fig. 3c. Data fitting with a linear function yields a stress coupling coefficient $2\alpha = 48 \pm 1$ MHz/GPa. This value is in very good agreement with recent first-principles calculations predicting $2\alpha = 49 \pm 2$ MHz/GPa for V_B^- centers embedded in a bulk hBN crystal[22]. The E-splitting remains almost unchanged though a slight reduction is observed at the highest applied pressures [see inset in Fig. 3c]. This effect, that cannot be explained by non-hydrostatic pressure components, is tentatively attributed to a decreased density of charges in the hBN crystal upon increasing pressure, which might result from pressure-induced charge state conversion of V_B^- centers.

Besides the hydrostatic shift of the magnetic resonances, our measurements also reveal that the contrast of the ODMR signal decreases with pressure [Fig. 3d] and fully vanishes above 3 GPa, a pressure at which the PL signal still remains easily detectable with a high signal-to-background ratio [Fig. 2b]. Such a reduction in ODMR contrast cannot be explained by a strain gradient within the hBN flake because the ODMR linewidth is not significantly modified by pressure (See Supplementary Fig. 2). The reduced ODMR contrast could simply result from a degradation of the platinum wire used for microwave excitation at high pressure. This hypothesis is excluded by microwave-free measurements of the longitudinal spin relaxation of V_B^- centers

https://doi.org/10.1038/s41467-025-63580-2

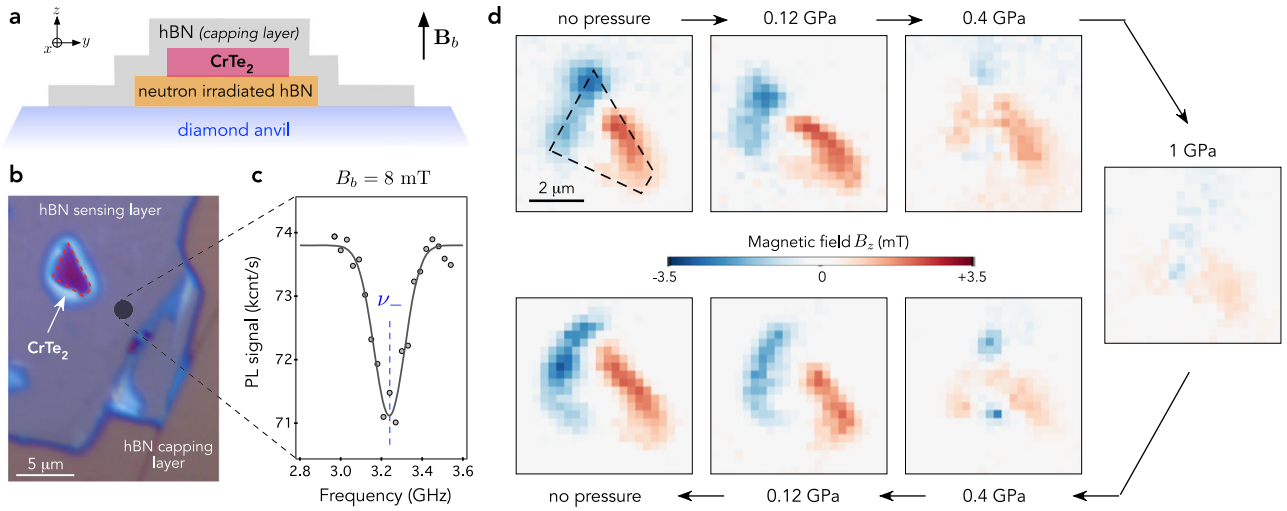

Fig. 4 | Magnetic imaging under pressure with V_B^- centers integrated in a van der Waals heterostructure. a Sketch and (**b**) optical image of the heterostructure deposited in the DAC chamber. All layers of the heterostructure are few tens of nanometers thick. **c** Spectrum of the low-frequency magnetic resonance of the V_B^- center recorded far from the $CrTe_2$ flake at zero external pressure with a bias field B_b = 8 mT. **d** Images of the magnetic field component B_z produced by the $CrTe_2$ flake for increasing (top) and decreasing (bottom) pressure. For all images, the pixel size is 300 × 300 nm^2 and the acquisition time per pixel is 60 s. The pixel-to-pixel noise estimated in small regions outside the $CrTe_2$ flake is around ~150 μT, a value roughly in line with the estimation of the magnetic sensitivity using ODMR spectra. All experiments are performed at room temperature with a green laser power of 2 mW.

[Fig. 3(e) and Methods]. At low pressure, the optically-detected spin relaxation curve is highly contrasted (~ 5%) and data fitting with an exponential decay yields a longitudinal spin decay time $T_1 = 5.1 \pm 0.1\,\mu$s. When pressure increases, T_1 is not significantly modified while the contrast of the spin decay strongly decreases and vanishes completely above 3 GPa [Fig. 3f]. These results confirm those obtained by ODMR spectroscopy. The spin readout contrast is linked to the combination of (i) an efficient polarization of the V_B^- center in the $|m_s = 0\rangle$ ground state by optical pumping and (ii) a spin-dependent PL emission. These two effects result from the spin selectivity of non-radiative ISC transitions to and from a metastable state during optical cycles[32–34]. While pressure-induced PL quenching discussed above is linked to an enhancement of non-radiative decay rates during optical cycles, the reduced ODMR contrast reveals a loss in spin selectivity of ISC transitions upon increasing pressure [Fig. 1b].

Magnetic imaging of a van der Waals magnet under pressure

Having established how the optical and spin properties of V_B^- centers in hBN evolve with hydrostatic pressure, we now turn to magnetic imaging under pressure with V_B^- centers integrated in a van der Waals heterostructure. As a proof of principle, we image the magnetic field produced by 1*T*-$CrTe_2$, a layered ferromagnet with in-plane magnetic anisotropy and a Curie temperature T_c ~320 K under ambient pressure[23–26]. The van der Waals heterostructure deposited inside the high-pressure chamber of the DAC is described by Figs. 4a, b. A thin hBN flake exfoliated from a neutron-irradiated crystal is first transferred on one of the diamond anvils and used as a magnetic detection layer. A micrometer-sized flake of $CrTe_2$ is then deposited on top of the sensing layer and capped with a hBN flake without V_B^- centers for protection. All layers of the heterostructure are few tens of nanometers thick.

In what follows, a bias magnetic field B_b = 8 mT is applied along the *z* axis to split the electron spin resonances of the V_B^- center via the Zeeman effect and we track the low-frequency component ν_- by ODMR spectroscopy. Neglecting the orthorhombic splitting parameter *E*, this frequency is given by $\nu_-(P) \approx D(P) - \gamma_e(B_b + B_z)$, where γ_e = 28 GHz/T is the electron spin gyromagnetic ratio and B_z denotes the magnetic field produced by the $CrTe_2$ flake along the *z* axis (See Supplementary Note 1). An ODMR spectrum recorded far from the ferromagnetic layer (B_z = 0) without applying external pressure is shown in Fig. 4c. From such a spectrum, the shot-noise limited magnetic field sensitivity η of the hBN-based sensing layer can be estimated by $\eta \approx 0.7 \times \frac{1}{\gamma_e} \times \frac{\Delta\nu}{\mathcal{C}\sqrt{\mathcal{R}}}$, where $\mathcal{R}$ is the rate of detected photons, $\mathcal{C}$ the ODMR contrast and $\Delta\nu$ the linewidth[40]. We obtain η ~400 μT/$\sqrt{\text{Hz}}$ for a diffraction-limited laser excitation spot below 1 μm^2. The same experiment performed at *P* = 1 GPa leads to a degraded magnetic sensitivity η ~ 800 μT/$\sqrt{\text{Hz}}$ due to the reduction in both spin readout contrast and PL signal (see Supplementary Fig. 3). Although NV centers implanted beneath the culet of a diamond anvil provide a better magnetic field sensitivity (~10 μT/$\sqrt{\text{Hz}}$) and can operate up to megabar pressure[16,17], the key advantage of the hBN-based sensing unit is its ability to be integrated in a van der Waals heterostructure, thus offering atomic-scale proximity to any type of 2D material placed in the high-pressure chamber of the DAC.

Magnetic field imaging is carried out by recording an ODMR spectrum at each point of a scan across the van der Waals heterostructure. By fitting the spectra, we infer the Zeeman shift of the spin resonance frequency, from which a map of the magnetic field component B_z is obtained. Images of the stray field distribution generated by the $CrTe_2$ flake at different pressures are shown in Fig. 4d. At low pressure, a magnetic field with reversed sign is mostly produced at opposite edges of the flake, as expected for a ferromagnetic material with uniform in-plane magnetization[26]. As pressure increases, the amplitude of the stray magnetic field reduces and almost vanishes at 1 GPa. The magnetic images also indicate a sudden variation of the stray field distribution around 0.4 GPa, which suggests the formation of magnetic domains within the flake that results from pressure-induced variations of magnetic interactions. This process is reversible, the initial magnetic configuration of the $CrTe_2$ flake being restored when the applied pressure is decreased [Fig. 4d]. Such measurements, which could not be carried out with conventional magnetometry techniques based on superconducting quantum interference devices (SQUID) or inductively coupled coils, illustrate the potential of V_B^- centers in hBN for in situ magnetic imaging of van der Waals magnets under pressure.

Analysis of the pressure-induced shift of the Curie temperature

The pressure-dependent magnetization of $CrTe_2$ is explained by a reduction of the magnetic exchange interaction upon increasing pressure, which leads to a decreased Curie temperature. In $CrTe_2$, the

https://doi.org/10.1038/s41467-025-63580-2

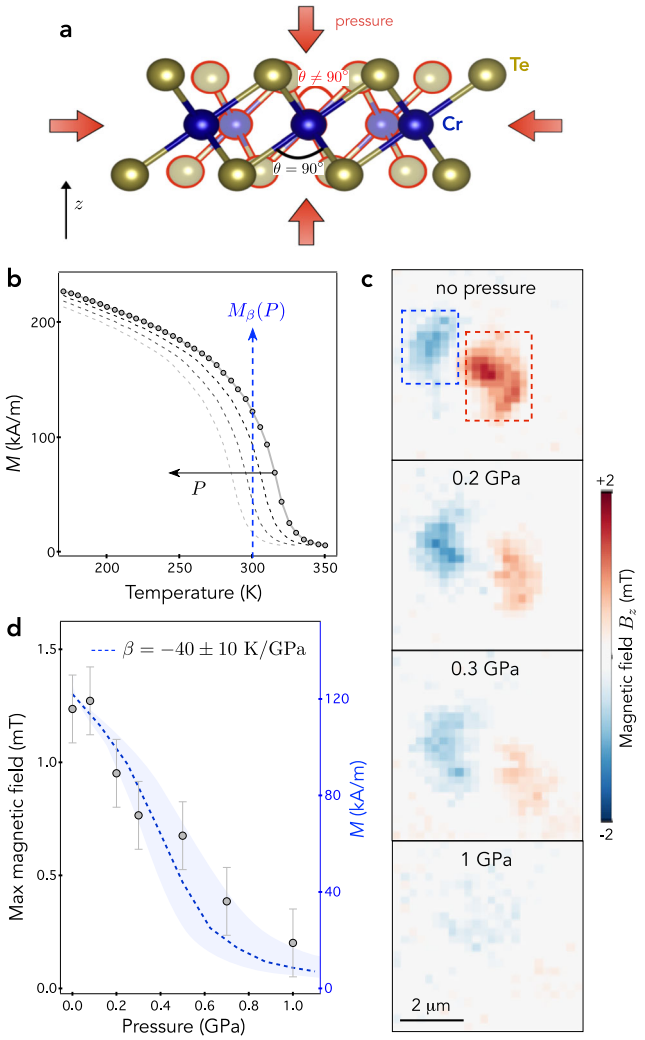

Fig. 5 | Pressure-induced shift of T_c. a Crystal structure of $CrTe_2$ illustrating the variation of the Cr-Te-Cr bond angle with applied pressure. **b** Temperature dependence of the magnetization M of a bulk $CrTe_2$ crystal recorded by vibrating sample magnetometry (circular markers). The dotted lines correspond to artificial shifts in the data to account for a pressure-induced shift in Curie temperature with a slope $\beta = dT_c/dP < 0$. The blue dashed line indicates the resulting pressure-dependent magnetization $M_\beta(P)$ at room temperature. **c** Pressure-dependent magnetic field map of a second $CrTe_2$ flake recorded at room temperature. The pixel size is 250 × 250 nm² and the acquisition time per pixel is 60 s. The magnetic field produced at the edges of the $CrTe_2$ flake is inferred within the regions indicated by the dashed rectangles in the top panel. In these regions, histograms of positive (red square) and negative (blue square) magnetic field values are fitted with a Gaussian function to obtain the maximum stray fields. **d** Maximum magnetic field measured at the edges of the $CrTe_2$ flake as a function of pressure. The error bars correspond to one standard deviation uncertainty. The shaded area correspond to the variation of M with pressure at room temperature, which is obtained by using the data shown in (**b**) and a pressure-induced shift of the Curie temperature $\beta = -40 \pm 10$ K/GPa.

exchange interaction between nearest Cr neighbors is dominated by the superexchange coupling mediated by a Te ion. The strength of this interaction is very sensitive to the angle θ of the Cr-Te-Cr bond. If $\theta = 90°$, the superexchange interaction is ferromagnetic with maximal coupling strength[6,7]. First principles calculations of the cell parameters of $CrTe_2$ indicate that θ is very close to 90° under ambient conditions (Methods). Upon increasing pressure, the angle θ decreases leading to a reduced strength of the superexchange coupling (see Supplementary Fig. 5), which in turn results in a decreased Curie temperature. A similar effect was reported for the van der Waals magnet $Cr_2Ge_2Te_6$[6] and for other $Cr_{1-\delta}Te$ compounds[41,42]. To obtain an estimate of the pressure-induced shift of the Curie temperature, we rely on the empirical analysis described in Fig. 5b. Using a measurement of the magnetization M of a bulk $CrTe_2$ crystal as a function of temperature, we first artificially infer its variations at room temperature by considering a pressure-induced shift of T_c with a slope $\beta = dT_c/dP < 0$ [Fig. 5b]. We then compare the resulting pressure-dependent magnetization curves $M_\beta(P)$ with the maximum magnetic field B_z produced at the edges of a $CrTe_2$ flake, which is proportional to the magnetization. This analysis is done for a series of magnetic images recorded at different pressure on a second heterostructure [Fig. 5c]. Note that an analysis of the spatial variation of the ODMR frequency away from the $CrTe_2$ flake does not reveal a significant spatial gradient of the in-plane stress component across the hBN sensing layer (see Supplementary Fig. 4). For this second $CrTe_2$ flake, we did not observe the formation of magnetic domains upon increasing pressure, making the comparison of the field at the edges more reliable. The results are shown in Fig. 5d. Our simple analysis reproduces fairly well the experimental results for $\beta = -40 \pm 10$ K/GPa.

To conclude, we have shown that V_B^- centers in hBN constitute a promising quantum sensing platform for local magnetic imaging in van der Waals heterostructures under hydrostatic pressures up to few GPa, a pressure range for which the properties of a wide variety of 2D magnets are efficiently altered[4–10]. Besides providing a new path for studying pressure-induced control of magnetic phases in 2D magnets, the hBN-based magnetic imaging unit also opens up interesting perspectives for exploring the physics of 2D superconductors[43] under pressure via local measurements of the Meissner effect. Of particular interest could be the study of superconductivity in twisted bilayer graphene, whose critical temperature is very sensitive to pressures in the GPa range[44]. After completion of this work, we became aware of complementary studies exploring the properties of V_B^- centers in hBN under pressure[45,46].

Methods

Diamond anvil cell (DAC)

All experiments were carried out with a membrane-driven DAC system equipped with two diamond anvils made of type-IIa single crystal diamonds with [100] crystalline orientation. The diamond anvils are cut into a 16-sided standard design with a culet diameter of 500 μm (Almax-easyLab). The sample chamber is defined by a hole (~250 μm diameter) drilled into a rhenium gasket, which is squeezed between the two opposing diamond anvils. The high-pressure chamber of the DAC was filled with a pressure-transmitting medium to provide a quasi-hydrostatic pressure environment. For the study of the optical properties of V_B^- centers under pressure, we used Daphne oil 7373, while for the study of its spin properties and for magnetic imaging under pressure, NaCl was employed as pressure transmission medium. The fluorescence spectrum of a ruby microcrystal loaded into the DAC chamber was used as a local pressure gauge[31]. In the pressure range considered in this work, we did not observe any broadening of the ruby emission lines (see Supplementary Fig. 1), as expected for a quasi-hydrostatic pressure environment.

To perform ODMR spectroscopy, a microwave excitation was delivered through a 10-μm wide platinum wire crossing the DAC chamber. For these measurements, the rhenium gasket was coated with a mixture of epoxy and boron nitride powder to make it insulating in order to minimize microwave losses.

Sample preparation

The hBN crystals studied in this work were synthesized by metal flux growth methods using a boron powder isotopically enriched with ^{10}B (99.2%) as precursor[27]. These crystals, which have a typical lateral size in the millimeter range and a thickness of a few tens of micrometers, were irradiated by thermal neutrons at the Ohio State University Research

Reactor to create V_B^- centers. Two different processes can lead to the creation of point defects via neutron irradiation: either by damages produced by neutron scattering through the crystal or by neutron absorption leading to nuclear transmutation[28]. The latter process strongly depends on the isotopic content of the hBN crystal. Indeed, ^{10}B has one of the highest neutron capture cross-sections of any isotope of any element in the periodic table, 3840 barns. In contrast, the neutron capture cross-sections for ^{11}B, ^{14}N and ^{15}N are all less than 2 barns, resulting in only weak interactions with thermal neutrons. As a result, neutron irradiation of a hBN crystal isotopically purified with ^{10}B ensures an efficient creation of boron vacancy-related defects throughout the entire volume of the hBN crystal via neutron transmutation doping[28].

The hBN crystal used to study the optical and spin properties of V_B^- centers under pressure was irradiated with a dose of ~2.6×10^{17} neutrons/cm^2. This crystal was cut into pieces with a lateral size of a few tens of micrometers, which were loaded inside the high-pressure DAC chamber. Magnetic imaging under pressure was performed with thin flakes exfoliated from a second hBN crystal, which was isotopically purified with ^{15}N to obtain a slight reduction of the ODMR linewidth[47–49]. This crystal was irradiated with a lower dose of ~1.4×10^{17} neutrons/cm^2.

The 1*T*-$CrTe_2$ crystal was synthesized using an elemental mixture of K, Cr and Te introduced under argon atmosphere (glove box) within an evacuated quartz tube. The quartz tube was heated to 1170 K for eight days, and slowly cooled-down[23]. The tubes were then opened in a glove box to prevent oxidation. Potassium de-intercalation was subsequently achieved by reaction of $KCrTe_2$ with a solution of iodine in acetonitrile. The resulting suspensions were stirred for about 1 h in an excess of iodine. Finally, filtering and drying under vacuum lead to 1*T*-$CrTe_2$ platelets with a lateral extension of few millimeters and a thickness of about 100 μm. The van der Waals heterostructure described in the main text was assembled in a glove box, using $CrTe_2$ flakes mechanically exfoliated from this bulk 1*T*-$CrTe_2$ crystal.

Scanning confocal microscope

The DAC system was incorporated into a home-built scanning confocal microscope operating under ambient conditions. A continuous laser excitation at 532 nm was focused onto the sample placed in the DAC chamber through a long-working distance microscope objective with a numerical aperture NA = 0.42 (Mitutoyo). The laser beam was scanned across the sample with a fast steering mirror (Newport, FSM-300) combined with a pair of telecentric lenses. The DAC system was placed on a translation stage equipped with a differential micrometer screw (Newport, DM-13L), which was used to adjust the focus of the laser beam onto the sample with a sensitivity of about 100 nm. The PL signal was collected by the same objective, focused in a single mode fiber and finally directed either to a spectrometer or to a silicon avalanche photodiode (APD) operating in the single photon counting regime (Excelitas, SPCM-AQRH). A 560 nm long pass filter was used for measurements of PL spectra and an additional bandpass filter (Semrock, 935/170) was inserted for measurements of the PL signal with the APD. To infer the excited-state lifetime of the V_B^- center, we used a pulsed laser source at 531 nm with a pulse duration of 60 ps (PicoQuant, PDL-800D). Time-resolved PL measurements were obtained by recording photon detection events on a time tagger with a bin width of 200 ps.

For ODMR measurements, a microwave synthesizer was followed by a 15 W power amplifier (Mini-circuits, ZHL-15W-422-S+) and connected to the platinum wire crossing the DAC chamber, which was terminated by a 50 Ω impedance. ODMR spectra were recorded by measuring the PL signal while sweeping the frequency of the microwave excitation.

T_1 measurements

The longitudinal spin relaxation time (T_1) of the V_B^- center was measured with the experimental sequence sketched in the top panel of Fig. 3e. A 5-μs-long laser pulse produced with an acousto-optic modulator was first used to polarize the V_B^- centers in the ground state $|m_s = 0\rangle$ by optical pumping. After relaxation in the dark during a variable time τ, the remaining population in $|m_s = 0\rangle$ was probed by integrating the spin-dependent PL signal produced at the beginning (500 ns window) of a second 5-μs-long laser pulse. This signal was normalized with a reference PL value obtained at the end of the first laser pulse. The longitudinal spin relaxation time T_1 was then inferred by fitting the decay of the normalized PL signal with an exponential function of the form $1 - C[1 - \exp(-\tau/T_1)]$, where C is the contrast of the optically-detected spin decay.

First-principles calculations

The atomic structure and the quasi-particle band structure of $CrTe_2$ have been obtained from DFT calculations using the VASP package[50,51]. The Perdew-Burke-Ernzerhof (PBE)[52] functional was used as an approximation of the exchange-correlation electronic term. Additionally DFT-D correction is applied to take into account van der Waals interactions[53]. The plane-augmented wave scheme[54,55] is used to treat core electrons, with twelve electrons for Cr atoms and six electrons for Te atoms in the valence states. To relax the structures upon hydrostatic pressure, the cell parameters are allowed to vary and all atomic positions are relaxed with a force convergence criterion below 0.005 eV/Å. A grid of $21 \times 21 \times 9$ k-points has been used, in conjunction with a Gaussian smearing with a width of 0.05 eV to determine partial occupancies. The cutoff energy of the plane-wave basis set was fixed to 500 eV. To determine magnetic states, the Hubbard U correction (PBE+U)[56] and spin-orbit coupling are included. The value of the U parameter was set as 5.8 eV as proposed in Ref. 57.

The calculated pressure-dependent lattice constants a and c of $CrTe_2$ are given in Supplementary Fig. 5 for hydrostatic pressures up to 2 GPa. The a and c lattice parameters are reduced by around 1% at 2 GPa. As a consequence the Cr-Cr distance is also decreasing, and the Cr-Te-Cr angle gets smaller than 90° with increasing pressure. Based on a Heisenberg model, we can estimate the nearest neighbor exchange coupling with a Hamiltonian that can be expressed as

$$\hat{\mathcal{H}} = -\sum_{ij} \hat{S}_x^{(i)} J \hat{S}_x^{(j)} + \sum_i A^{(i)} \left(\hat{S}_z^{(i)}\right)^2, \tag{3}$$

where J is the effective exchange coupling constant, $\hat{\mathbf{S}} = (\hat{S}_x, \hat{S}_y, \hat{S}_z)$ is the spin vector, and $A^{(i)}$ is the magnetic anisotropy of a single ion. To calculate J one can use energy difference between the ferromagnetic (FM) and antiferromagnetic (AFM) configurations simulated in $2 \times 2 \times 1$ supercell, since $E_{FM} = E_o - 12JS_x^2$ and $E_{AFM} = E_o + 4JS_x^2$, where E_o is the total energy of systems without magnetic coupling. At 0 GPa, the magnetic moment of each Cr atom is 3.586 μ_B, and the effective J of monolayer is 2.24 meV. When pressure is increased those values decrease (see Supplementary Fig. 5).

Data availability

The datasets generated as part of the current study are available from the corresponding author upon request.

Code availability

The codes used for the analysis included in the current study are available from the corresponding author upon request.

References

1. Gibertini, M., Koperski, M., Morpurgo, A. F. & Novoselov, K. S. Magnetic 2D materials and heterostructures. *Nat. Nanotechnol.* **14**, 408–419 (2019).
2. Wang, Q. H. et al. The magnetic genome of two-dimensional van der Waals materials. *ACS Nano* **16**, 6960–7079 (2022).

3. Yang, H. et al. Two-dimensional materials prospects for non-volatile spintronic memories. *Nature* **606**, 663–673 (2022).
4. Song, T. et al. Switching 2D magnetic states via pressure tuning of layer stacking. *Nat. Mater.* **18**, 1298–1302 (2019).
5. Li, T. et al. Pressure-controlled interlayer magnetism in atomically thin CrI_3. *Nat. Mater.* **18**, 1303–1308 (2019).
6. Sun, Y. et al. Effects of hydrostatic pressure on spin-lattice coupling in two-dimensional ferromagnetic $Cr_2Ge_2Te_6$. *Appl. Phys. Lett.* **112**, 072409 (2018).
7. Mondal, S. et al. Effect of hydrostatic pressure on ferromagnetism in two-dimensional CrI_3. *Phys. Rev. B* **99**, 180407 (2019).
8. Lin, Z. et al. Pressure-induced spin reorientation transition in layered ferromagnetic insulator $Cr_2Ge_2Te_6$. *Phys. Rev. Mater.* **2**, 051004 (2018).
9. Wang, H. et al. Pressure-dependent intermediate magnetic phase in thin Fe_3GeTe_2 flakes. *J. Phys. Chem. Lett.* **11**, 7313–7319 (2020).
10. Pawbake, A. et al. Magneto-optical sensing of the pressure driven magnetic ground states in bulk CrSBr. *Nano Lett.* **23**, 9587–9593 (2023).
11. Doherty, M. W. et al. Electronic properties and metrology applications of the diamond NV^- center under pressure. *Phys. Rev. Lett.* **112**, 047601 (2014).
12. Lesik, M. et al. Magnetic measurements on micrometer-sized samples under high pressure using designed NV centers. *Science* **366**, 1359–1362 (2019).
13. Hsieh, S. et al. Imaging stress and magnetism at high pressures using a nanoscale quantum sensor. *Science* **366**, 1349–1354 (2019).
14. Yip, K. Y. et al. Measuring magnetic field texture in correlated electron systems under extreme conditions. *Science* **366**, 1355–1359 (2019).
15. Shang, Y.-X. et al. Magnetic sensing inside a diamond anvil cell via nitrogen-vacancy center spins. *Chin. Phys. Lett.* **36**, 086201 (2019).
16. Wang, M. et al. Imaging magnetic transition of magnetite to megabar pressures using quantum sensors in diamond anvil cell. *Nat. Commun.* **15**, 8843 (2024).
17. Bhattacharyya, P. et al. Imaging the Meissner effect in hydride superconductors using quantum sensors. *Nature* **627**, 73–79 (2024).
18. Gottscholl, A. et al. Initialization and read-out of intrinsic spin defects in a van der Waals crystal at room temperature. *Nat. Mater.* **19**, 540–545 (2020).
19. Huang, M. et al. Wide field imaging of van der Waals ferromagnet Fe_3GeTe_2 by spin defects in hexagonal boron nitride. *Nat. Commun.* **13**, 5369 (2022).
20. Kumar, P. et al. Magnetic imaging with spin defects in hexagonal boron nitride. *Phys. Rev. Appl.* **18**, L061002 (2022).
21. Healey, A. J. et al. Quantum microscopy with van der Waals heterostructures. *Nat. Phys.* **19**, 87–91 (2023).
22. Udvarhelyi, P. et al. A planar defect spin sensor in a two-dimensional material susceptible to strain and electric fields. *npj Computational Mater.* **9**, 150 (2023).
23. Freitas, D. C. et al. Ferromagnetism in layered metastable 1*T*-$CrTe_2$. *J. Phys.: Condens. Matter* **27**, 176002 (2015).
24. Sun, X. et al. Room temperature ferromagnetism in ultra-thin van der Waals crystals of 1*T*-$CrTe_2$. *Nano Res.* **13**, 3358–3363 (2020).
25. Purbawati, A. et al. In-plane magnetic domains and Néel-like domain walls in thin flakes of the room temperature $CrTe_2$ van der waals ferromagnet. *ACS Appl. Mater. Interfaces* **12**, 30702 (2020).
26. Fabre, F. et al. Characterization of room-temperature in-plane magnetization in thin flakes of $CrTe_2$ with a single-spin magnetometer. *Phys. Rev. Mater.* **5**, 034008 (2021).
27. Liu, S. et al. Single crystal growth of millimeter-sized monoisotopic hexagonal boron nitride. *Chem. Mater.* **30**, 6222–6225 (2018).
28. Li, J. et al. Defect engineering of monoisotopic hexagonal boron nitride crystals via neutron transmutation doping. *Chem. Mater.* **33**, 9231–9239 (2021).
29. Haykal, A. et al. Decoherence of V_B^- spin defects in monoisotopic hexagonal boron nitride. *Nat. Commun.* **13**, 4347 (2022).
30. Klotz, S., Chervin, J.-C., Munsch, P. & Marchand, G. L. Hydrostatic limits of 11 pressure transmitting media. *J. Phys. D: Appl. Phys.* **42**, 075413 (2009).
31. Mao, H. K., Xu, J. & Bell, P. M. Calibration of the ruby pressure gauge to 800 kbar under quasi-hydrostatic conditions. *J. Geophys. Res.: Solid Earth* **91**, 4673–4676 (1986).
32. Baber, S. et al. Excited state spectroscopy of boron vacancy defects in hexagonal boron nitride using time-resolved optically detected magnetic resonance. *Nano Lett.* **22**, 461–467 (2022).
33. Clua-Provost, T. et al. Spin-dependent photodynamics of boron-vacancy centers in hexagonal boron nitride. *Phys. Rev. B* **110**, 014104 (2024).
34. Whitefield, B., Toth, M., Aharonovich, I., Tetienne, J.-P. & Kianinia, M. Magnetic field sensitivity optimization of negatively charged boron vacancy defects in hBN. *Adv. Quantum Technol.* **n/a**, 2300118 (2023).
35. Carbone, A. et al. Quantifying the creation of negatively charged boron vacancies in He-ion irradiated hexagonal boron nitride. *Phys. Rev. Materials* **9**, 056203 (2025).
36. Gong, R. et al. Coherent dynamics of strongly interacting electronic spin defects in hexagonal boron nitride. *Nat. Commun.* **14**, 3299 (2023).
37. Durand, A. et al. Optically active spin defects in few-layer thick hexagonal boron nitride. *Phys. Rev. Lett.* **131**, 116902 (2023).
38. Ivády, V. et al. Ab initio theory of the negatively charged boron vacancy qubit in hexagonal boron nitride. *npj Computational Mater.* **6**, 41 (2020).
39. Gracheva, I. N. et al. Symmetry of the hyperfine and quadrupole interactions of boron vacancies in a hexagonal boron nitride. *J. Phys. Chem. C.* **127**, 3634–3639 (2023).
40. Dréau, A. et al. Avoiding power broadening in optically detected magnetic resonance of single NV defects for enhanced dc magnetic field sensitivity. *Phys. Rev. B* **84**, 195204 (2011).
41. Ohta, S., Kanomata, T., Kaneko, T. & Yoshida, H. Pressure effect on the curie temperature and thermal expansion of CrTe. *J. Phys.: Condens. Matter* **5**, 2759 (1993).
42. Ishizuka, M. et al. Pressure-induced magnetic phase transition in CrTe at approximately 7 GPa. *J. Alloy. Compd.* **320**, 24–28 (2001).
43. Qiu, D. et al. Recent advances in 2D superconductors. *Adv. Mater.* **33**, 2006124 (2021).
44. Yankowitz, M. et al. Tuning superconductivity in twisted bilayer graphene. *Science* **363**, 1059–1064 (2019).
45. He, G. et al. Probing stress and magnetism at high pressures with two-dimensional quantum sensors. *Nat. Commun.* **16**, 8162 (2025).
46. Yu, L.-X. et al. Magnetic measurements under high pressure with a quantum sensor in Hexagonal Boron Nitride. Preprint at https://doi.org/10.48550/arXiv.2501.13757 (2025).
47. Janzen, E. et al. Boron and nitrogen isotope effects on hexagonal boron nitride properties. *Adv. Mater.* **36**, 2306033 (2024).
48. Clua-Provost, T. et al. Isotopic control of the boron-vacancy spin defect in hexagonal boron nitride. *Phys. Rev. Lett.* **131**, 126901 (2023).
49. Gong, R. et al. Isotope engineering for spin defects in van der Waals materials. *Nat. Commun.* **15**, 104 (2024).
50. Kresse, G. & Hafner, J. Ab initio molecular dynamics for liquid metals. *Phys. Rev. B* **47**, 558–561 (1993).
51. Kresse, G. & Furthmüller, J. Efficient iterative schemes for ab initio total-energy calculations using a plane-wave basis set. *Phys. Rev. B* **54**, 11169–11186 (1996).
52. Perdew, J. P., Burke, K. & Ernzerhof, M. Generalized gradient approximation made simple. *Phys. Rev. Lett.* **77**, 3865–3868 (1996).
53. Grimme, S., Antony, J., Ehrlich, S. & Krieg, H. A consistent and accurate ab initio parametrization of density functional dispersion

correction (DFT-D) for the 94 elements H-Pu. *J. Chem. Phys.* **132**, 154104–19 (2010).
54. Blöchl, P. E. Projector augmented-wave method. *Phys. Rev. B* **50**, 17953 (1994).
55. Kresse, G. & Joubert, D. From ultrasoft pseudopotentials to the projector augmented-wave method. *Phys. Rev. B* **59**, 1758–1775 (1999).
56. Dudarev, S. L., Botton, G. A., Savrasov, S. Y., Humphreys, C. J. & Sutton, A. P. Electron-energy-loss spectra and the structural stability of nickel oxide: An lsda+u study. *Phys. Rev. B* **57**, 1505–1509 (1998).
57. Liu, Y., Kwon, S., de Coster, G. J., Lake, R. K. & Neupane, M. R. Structural, electronic, and magnetic properties of $CrTe_2$. *Phys. Rev. Mater.* **6**, 084004 (2022).

Acknowledgements

The authors thank Manuel Nuñez-Regueiro for valuable discussions. This work was supported by the French Agence Nationale de la Recherche through the program ESR/EquipEx+ 2DMAG (grant number ANR-21-ESRE-0025), the program PEPR SPIN (ANR-22-EXSP-0008), the projects Qfoil (ANR-23-QUAC-0003) and NEXT (ANR-23-CE09-0034), and the Institute for Quantum Technologies in Occitanie. hBN crystal growth was supported by the Materials Engineering and Processing program of the National Science Foundation, award number CMMI 1538127 and by the Office of Naval Research award N00014-22-1-2582. Neutron irradiation of the hBN crystal was supported by the U.S. Department of Energy, Office of Nuclear Energy under DOE Idaho Operations Office Contract DE-AC07-051D14517 as part of a Nuclear Science User Facilities experiment. I.C.G. acknowledges the computer resources through the "Calcul en Midi-Pyrénées" initiative CALMIP (projects p0812) and CINES, IDRIS, and TGCC under the allocation 2024-A0160906649 made by GENCI, and the French Agence Nationale de la Recherche under grant agreement ANR-23-QUAC-004 (EXODUS) for financial support.

Author contributions

Z.M., A.D., S.C., A.F., B.G., G.C. and V.J. conducted and analyzed the experiments. J.F., Z.M., C.R., X.M., S.C. and J.R. prepared the van der Waals heterostructures at the culet of a diamond anvil. A.H.-A., N.R, and J.C. synthesized and characterized the bulk $CrTe_2$ crystal. I.C.G. carried out the first-principles calculations. J.L., T.P. and J.H.E. performed the hBN crystal growth. V. J. coordinated the project and wrote the manuscript. All the authors discussed the data and commented the manuscript.

Competing interests

The authors declare no competing interests.

Additional information

Supplementary information The online version contains supplementary material available at https://doi.org/10.1038/s41467-025-63580-2.

Correspondence and requests for materials should be addressed to V. Jacques.

Peer review information *Nature Communications* thanks Gang-Qin Liu, and the other, anonymous, reviewers for their contribution to the peer review of this work.